tmp title: MUSC source

Damien Pageot[*][†]**, Donatienne Leparoux**[*]**, Mathieu Le Feuvre**[*]**, Olivier**

Durand[*] **and Yann Capdeville**[‡]

[*]*LUNAM-IFSTTAR,*

[†]*OSUNA*

[*]*LPGN,*

(December 14, 2015)

GEO-Example

Running head: ***Geophysics*** example

ABSTRACT

INTRODUCTION

Since the early developments of seismic imaging methods in the middle of 20th century, approaches and algorithms innovations are still proposed in current research projects. The improvements deal with both the qualitative imaging techniques like migration (e.g. Berkhout et al. (2012); Guofeng et al. (2013)), novel applications of quantitative imaging methods such as the first arrival tomography (e.g. Bohm et al. (2015)), or even more recent approaches like the Full Waveform Inversion (e.g. Perez Solano et al. (2014), see Virieux and Operto (2009) for a revue of this last decade). The refinements are proposed for different scales like near surface applications for civil engineering topics or more deeper investigation for example for oil prospection or crustal imaging at regional or global scales. They are mostly validated by using synthetic data, for example with well known shared benchmark (like the Marmousi case). However, the synthetic data are generally computed using the same wave propagation modeling engine used in the inverse problem process. In other terms, the synthetic data are computed with some assumptions which are the same in the inverse problem, for example the approximation of acoustic propagation, a 2D space medium, or a 2D line source. This approach, called *inverse crime* (Wirgin, 2004) is particularly useful for validating an algorithm in its early development stage but does not take into account the artefacts that can be due to the assumptions of the direct problem. Some authors tackle this issue by providing 3D data which are inverted with a 2D approach or other restrictive assumptions (e.g). But also in this case, the approach does not allow to assess the efficiency of the method for real seismic data. Moreover, because no one knows precisely the Earth interior, it is difficult to evaluate the capacity of a method to recover physical parameters and structures from real seismic data which can lead sometimes to geological misinterpretation due to numerical artifacts (Morozov, 2004). Thus, it is necessary to add

a step for which imaging methods will be tested for experimental seismic measurements obtained under controlled conditions.

The best way to satisfy this need is to use Physical Small Scale Modeling Methods (noted *PSM* subsequently). *PSM* were used since several years to study the propagation of waves in various media with several stage of complexity, from acoustic wave propagation in homogeneous media to elastic wave propagation in three-dimensional heterogeneous anisotropic media (Rieber, 1936; Howes et al., 1953; Hilterman, 1970; French, 1974; Bishop et al., 1985; Pratt, 1999; Favretto-Cristini et al., 2013; Sarkar et al., 2003; Isaac and Lawton, 1999), and allow to generate experimental seismic data under well-controlled conditions. In this way, recent studies have been conducted to simulate multi-sources and multi-receivers through piezo-electric transducers (Wong et al., 2009). An alternative approach consists in using the laser interferometry as the receiver system, as done in the MUSC Laboratory (Bretaudeau et al., 2008, 2011, 2013), *Mesure Ultrasonore Sans Contact* in French. This technology, by avoiding the contact of the receivers on the model, allows to by-pass the coupling issue of transducers that is difficult to model. In this way, the MUSC laboratory is designed to simulate (1) wide-angle on-shore acquisitions modeling both body waves and surface waves, (2) automatic multisource-multireceiver measurements with a high-productivity, (3) high-precision source-receiver positioning and (4) high-precision recording of absolute surface displacement without coupling effects.

These abilities have been validated through a comparison of experimental data to numerical simulation in a 2-dimensions space containing a cavity (Bretaudeau et al., 2011). The results showed very fine similarities concerning the diffracted and converted arrivals when the source waveform is taken into account. For that, the numerical source was simulated in 2D and some corrections were required to compare the amplitude results, with some

3

remaining weak discrepancies as mentioned in the discussion of (Bretaudeau et al., 2011).

Moreover, the source diagram was assessed with a parallel measurement bench, showing an

50 omnidirectional propagation but the repeatability of the source impact was not studied.

Our objective here is to increase the potential of the MUSC system as a reliable tool for generating experimental data which will be distributed in the scientific community. Thus, we present two studies of experimental data in order to : 1) quantitatively refine the comparison between numerical and experimental data by taking into account the 3D/2D

55 geometrical spreading effects through an alternative way and 2) identify the reproducibility of the source impact and, consequently, data repeatability. These approaches will complete the knowledge of the system and facilitate the achievement of massive multi-source and multi-receiver data simulating subsurface seismic experimental campaigns. Moreover, they provide quantitative informations about the data quality for geophysicists who need to use

60 them measurement based on reduced scale model.

In order to achieve these objectives, we used a seismic wave modeling code based on the Spectral Element Method (Komatitsch et al., 1998; Komatitsch and Tromp, 1999; Komatitsch et al., 2005; Festa and Vilotte, 2005) that allows to provide numerical signals as reference data for comparison. The Spectral Element Method (SEM) has several advantages

65 compared to finite differences and finite elements, such as: (1) a weak formulation which can naturally take into account the free surface, (2) an explicit scheme in time domain facilitating parallelization and reducing the computational cost, (3) a spatial discretization (mesh) convenient for the representation of complex environments and (4) high precision results and low numerical dispersion.

70 The numerical characteristics of the code used are described in a first part below. After-

wards, the specificities of the MUSC system are explained, followed by the presentation of the models used. Finally The two coupled studies on experimental data are detailed, in the respective aims (1) of refining the comparison between numerical and experimental data by taking into account the geometrical spreading effects between two-dimensional and three-dimensional data through an alternative way, and (2) of identifying the reproducibility of the source impact to validate the data reproducibility.

METHODS

Numerical modeling: Spectral Element Method

Various numerical methods exist to resolve the equation of motion in arbitrary elastic media. The most widely used for seismic applications is the Finite-Differences (FD) method (Virieux, 1986; Levander, 1988; Robertsson et al., 1994; Pratt, 1990; Stekl and Pratt, 1998; Saenger and Bohlen, 2004) which estimates each derivative on a regular Cartesian grid using a Taylor development (Moczo et al., 2004) of order n. FD is simple to implement and robust but shows some limitations. First the Cartesian grid is defined by the minimum propagated wavelength (λ_{min}) in the full medium which conducts to a very small spatial step in case of low velocities zones as it is usually the case for subsurface issues. Moreover, Saenger et al. (2000) show that 60 points by wavelength (λ) are needed to correctly model propagation of Rayleigh wave in order $n = 2$ where only 15 points by λ are required to correctly model propagation of body waves which increases drastically the numerical cost in case of near-surface modeling experiments. Second, the Cartesian grid does not provide a suitable tool to reproduce properly complex topography and interfaces.

To overcome this limit, one can use the Finite-Elements Method (FEM) which is another

5

popular method used for wave propagation modeling (Lysmer and Drake, 1972; Seron et al., 1990; Hulbert and Hughes, 1990). FEM is based on a variational formulation of the equation of motion and gives a continuous approximate solution in space using polynomial basis functions defined on each node of each cell of the mesh. The natural boundary conditions of FEM is the free surface and the triangular (in 2D) or tetraedric (in 3D) unstructured meshes are well adapted to complex media and topography. However, low polynomial basis are inadequate with fine spatial discretization and the required discretization to obtain precise and non-dispersive solution is numerically costly.

Parallel, at the end of the 20th century, the Spectral Element Method (SEM), widely used in fluid dynamics (Patera, 1984; Korczak and Patera, 1986; Karniadakis, 1989), has been adapted to seismic wave propagation (Komatitsch et al., 1998; Komatitsch and Tromp, 1999; Komatitsch et al., 2005; Festa and Vilotte, 2005). The SEM is a variant of FEM based on a high-order piecewise polynomial approximation of the weak formulation of the wave equation which leads to a spectral convergence ratio as the interpolation order increases.

In this method, the wave-field is formulated in terms of high-degree Lagrange interpolants, and the integrals calculation are based on the quadrature of Gauss-Lobatto-Legendre (gll). This combination leads to a perfectly diagonal mass matrix which provides in turn a fully explicit time scheme suitable for numerical simulations on parallel computers.

SEM inherits the flexibility and the natural free surface condition of the FEM (Tromp et al., 2008). The typical element size that is required to generate an accurate mesh is of the order of λ, λ being the smallest wavelength of waves propagated in the model. In our study, the models are meshed with quadrangles (2D) and hexaedras (3D) using the open-source software package GMSH (Geuzaine and Remacle, 2009). It is particularly well suited

6

to handle complex geometries and interface matching conditions (Cristini and Komatitsch, 2012). In order to simulate infinite or semi-infinite domain, SEM can use Perfect Match Layers boundary conditions (Bérenger, 1994; Festa and Vilotte, 2005). However they are not used here because we simulate scale models which are spatially limited for the use in the MUSC system. The latter is described below in terms of technical specifications.

Physical modeling: MUSC system

The MUSC system (Bretaudeau et al., 2008, 2011, 2013) is built to experimentally reproduce field seismic data with a great accuracy on reduceds scale model. Figure 1 shows the measurement bench and its components : it is composed of a honeycomb tab and two arms which control the source and the receiver positions with a precision of 10 μm.

The receiving system of MUSC system is a laser interferometer based on a phase shift of the reflected laser signal due to the particular displacement at the surface of the model during the seismic waves propagation in the medium. An integrated real-time calibration system enables a continuous conversion to a quantitative measure of the particular displacement. The diameter of the laser beam on the model surface equals 20 micrometers for the focal distance of 40 mm and allows a detection of a vertical displacement of the order of the nanometer in the frequency range from 10 kHz to 20 MHz. The laser interferometer constitutes a non-coupled receiver which avoids the complicated modeling of the coupling effects on measurement.

But using a laser source needs more security protocols in the laboratory and up to now, the seismic source in the MUSC laboratory is simulated by a piezoelectric transducer linked to a launching and synchronization system. It allows to choose the source function, i.e.,

a waveform like a Gauss or Ricker function, the central frequency f_0 and the time delay t_0. For that, the source is generated by a waveform generator and is then amplified before being transmitted to the small-scale-model.

For the purpose of reduced scale modeling, the change of scale must keep the relationship between observables, i.e. amplitudes and time arrivals. Concerning the amplitude, the quality factor Q will be chosen to be in the same range as the materials of near surface. For the time arrivals, the key parameter is the rate between the propagated seismic wavelength and the spatial dimensions of the experience that includes the model geometry, the spatial increment between the sources and the receivers positions, but also the dimensions of the source impact. In the framework of seismic physical modeling, this latter must be as close as possible to a point source in order to simulate the spatial energy repartition of a weight drop at the soil surface, i.e. with an isotropic directivity of the emitted P waves.

In the MUSC system, the main frequency bands used for reduced scale data are [20 KHz ; 200 KHz] and [300 KHz; 800 KHz], respectively called here "low frequency band" and" high frequency band". For the lower spectral band, a commercial piezo-electric transducer is used without any coupling gel. For the higher band, the piezoelectric source is coupled through a conical adapter which is sticked to the transducer in order to obtain the expected impact surface. The resulting source pattern is isotropic enough in the spectral band of interest (see (Bretaudeau et al., 2011) for more details).

The lower frequency band is well adapted to simulate seismic experiment applied to near surface through the scales ratios proposed in tables 1 and 2. In the first case (table 1), a central frequency of 100 KHz in the laboratory corresponds to a central frequency of 100 Hz on the field, whereas in the second one (table 2) a central frequency of 100 KHz in the

8

laboratory corresponds to a central frequency of 50 HZ on the field. Note that with these propositions, the quality factor Q and the density ρ are modeled with a ratio equal to 1, i.e. they remain the same at both of the scales. Actually small-scale models are generally made of thermoplastic or casting epoxy resin materials (Bretaudeau et al., 2013, 2011, 2008).The mechanical properties of these materials provide attenuation characteristics close to natural soil materials of subsurface media. Their seismic velocities are about 2 times of those in subsurface materials as proposed in table 2. The possibilities of combinations can generate the impedance contrasts encountered in the geophysical issues.

The MUSC bench presented above has been studied for simulating with a great reproducibility the typical field campaigns of subsurface seismic measurement. The validation was achieved by comparison between small scale measurement and numerical data (ref). Results have shown a great reproducibility of the converted and diffracted events recorded on the vertical component. The amplitudes analysis had been conducted through 2D-3D corrections and small discrepancies remained due to the difficulty of taking into account the S and P waves in the same way. For this reason, we propose here to refine the study by testing a more recent correction methodology (ref) as well as providing experimental and numerical, 2D and 3D data. This study will be achieved through data carried out on two models that are presented below.

Characteristics of the scale models tested

In this study, we consider two different reduced scale models. The first one is homogeneous whereas the second one contains a deeper layer with a geometrical variation of the interface along the profile. The top layer, as well as the entire first model, is made of epoxy-resin

9

called F50. The deeper layer is built with a more dense resin called LAB1000. The latter model is called Bialt. The specific properties of these two kind of resins are summarized in the table 3. As required, note that the Q-factor values are of the same order of the Q-factor value in the shallowest parts of the natural media.

As described in the previous part and proposed in table 2, it is possible to take into account a scale ratio equal to 2 for the velocities, and use a 100 KHz Ricker source in order to simulate a 50 Hz Ricker source in reality. This seems realistic for simulating an hammer impact on the soil. In this case, the distance scale ratio is 1000 such that a 1 mm distance in the laboratory experiment corresponds to a 1 m distance in reality. Following these rules, we propose different shot described in the following part.

The recorded signals will be finely analyzed for a maximum offset equal to 60 mm in the case of the homogeneous model and 100 mm for the bialt model. Thus, the resin models have to be big enough in order to carry out this receiver-source distances without providing boundary echoes which could interfere with the direct arrivals. For that, the homogeneous model is 500 mm long and 504 mm large and 115 mm high. The Bialt model is 300 mm large and 200 mm high. The interface geometry is presented in figure 3. It simulates an interface between a 3 m thick layer of clay overcoming a limestone layer.

The numerical meshing required for numerical simulations involve dimensions of cells about The resulting meshing structure for the bialt model is presented figure. There is no PML in order to really simulate the reflexions due to the model boundaries.

These two resin blocks as well as their corresponding numerical models will be used for generating seismic data with punctual sources but also line sources in order to study the effective wavelet really emitted in the MUSC bench and its reproducibility as described in

10

the two next parts.

RESULTS

From point-source to line-source response

In the framework of wave propagation modeling and imaging methods, most of available algorithms are limited to the two-dimensional approximation especially for computational cost causes. More, a widely used way to validate imaging methods consists in inverse crime while the validity of applications on real dataset is conditioned by strong *a priori* and a weak knowledge of the target. All of these leads to a limited validation of the efficiency of imaging methods to recover parameter models. Thus, it is critical for two-dimensional inversion of field data to accurately correct the difference between two-dimensional and three-dimensional geometrical spreading.

Point-source data can be corrected from geometrical spreading using a simple two-steps signal processing: (1) convolving each trace by $\sqrt{t^{-1}}$, where t is the time, to correct the phase shift of $\pi/4$ (2) applying a taper $\sqrt{t}$ to all traces to correct relative amplitudes. Some variation exist, for examples, using a linear source wavelet estimation method to correct the phase (Bretaudeau et al., 2013) or applying an offset conditioning to obtain a better correction of amplitudes (Tran et al., 2013). To correct some biases of these methods, Forbriger et al. (2014) and Schafer et al. (2014) have introduced, and successfully applied to synthetic data, the *hybrid method*. In the *hybrid method* the geometrical spreading correction is conditioned by: (1) the offset, (2) the knowledge of the wave propagation velocities in the medium and (3) a user defined ratio used to smoothly correct amplitudes from near offset, which used the direct wave correction, to far offsets, which used th single

11

velocity correction. This method is efficient but difficult to calibrate without reference data. Then, results are thus strongly dependent of user's *a priori* and attempts. More, this kind of signal correction is mostly valid for one-dimensional medias, two-dimensional (x, z) medias with precautions, invariant along the y-axis.

In other cases, 3D data are corrected or process *on the fly*, or used as is in algorithm using a 2.5D approximation.

Thus, the missing step between purely numerical validation and real data applications can be the use of experimental line-source seismograms recorded under controlled conditions. Here, we take advantage of the experimental framework to explore an alternative approach specific to MUSC system. Figure 4 presents a schematic representation of the principle for this kind of experiment composed of a finely-sampled line of point-source and a line of receiver for each considered offset. Theoretically, the weighted stack of all receiver with the same offset will results in a pseudo line-source response. Taking advantage of the reciprocity principle the experiment can be simplified by considering only one receiver per offset, on a line perpendicular and centered to the defined line-source. All traces of each common receiver gather are then stacked together to obtain the line-source response. In order to apply this protocol, we have to choose a line-source's length L sufficiently great to be assimilated to a cylindrical source and above all a suitable sampling interval Δs between each point-source constituting the pseudo line-source to ensure applicability of the *Huygen's principle.*

For this experiment, we choose the homogeneous block of *F50 pure* epoxy-resin. Given the material's properties, we choose $L = 240\ mm$ and $ds = 0.5\ mm$ which leads to 481 point-source locations. Four receiver positions have been selected: 45, 50, 55 and 60 mm

offset. The source wavelet is a Ricker with a central frequency $f_0 = 100 \ kHz$ and $t_0 =$ 0.03 ms. Figures 5(a,c) show the signal recorded at one receiver for a line of point-sources and for both two-dimensional and three-dimensional numerical modeling (figure 5(a)) and experimental modeling (figure 5(b)). Note that the quality factor is not took into account for the numerical modeling. The numerical result (fig 5(a)) clearly shows the different attempted P and S wavefronts and the reflected PP and P-SV wavefronts while for the experimental result, the PP-reflected wavefront is altered by the echo of the experimental source (which will be considered in the next section). Here, the point-source response corresponds to the central trace (distance 0 mm) and the equivalent line-source response is the weighted stack of all traces. Comparisons of the point-source and line-source responses are presented in figures 5(b) and 5(d), respectively for numerical and experimental modeling. For numerical modeling, we provide a line-source response from two-dimensional modeling in comparison of both three-dimensional and weighted stack results. Note that traces are here normalized to be comparable. These comparisons show clearly the attempted phase shift of $\pi/4$ between point-source and line-source responses, and some differences in terms of waveform, especially for the experimental results between 0.08 and 0.10 ms. More, the response from two-dimensional modeling perfectly fit the weighted stack result appart from 0.18 ms to the end of the time window where the PSv wave amplitude is abnormally high. This effect can be related to limited dimensions in time and space of the original three-dimensional signal.

The same comparisons, for the four source-receiver offsets, are shown in figures 6(a) and 6(b) for numerical modeling and experimental modeling, respectively. To validate our approach to produce experimental line-source responses, we have applied and calibrated the *hybrid method* (Forbriger et al., 2014; Schafer et al., 2014) on the numerical point-source response

to obtain the equivalent line-source response. Figure 6(b) presents the comparison between numerical line-source response and equivalent line-source response and shows that the *hybrid* method is able to produce the equivalent line-source response with a very good agreement in terms of both phase and amplitude for P and S -waves but not for PP and PSv reflected waves. Finally, we have applied the correction with the same calibration to the experimental signal (figure 6(d)). This last result shows a good agreement between experimental line-source and equivalent line-source responses up to 0.12 *ms*. Then, the correction of the geometrical spreading seems unable to scale correctly amplitude where echo of the source and reflected wave are superimposed. For the signal at 55 *mm* offset, the largest amplitude difference can be explain by a weaker *signal-to-noise* ratio than for the the three other offsets in the experimental data.

These results on our approach to generate experimental line-source responses show that the MUSC system is efficient and can produce reliable 2D experimental data suitable for migration-based methods such as FWI.

Experimental source reproducibility

In the framework of high-resolution imaging, such as FWI, first validations of the method are general performed on the basis of inverse crime or using synthetic data from an other modeling code. In these cases, the source waveform is known and the initial model m_0 is generally a smoothed version of the true model used in the forward modeling to obtain synthetic observed data. Consequently, no source wavelet estimation is done. However, the knowledge of the source waveform is an important task when real data are inverted. In many cases, efficient sources are recovered using a linear source wavelet estimation method

(Pratt, 1999) which integrate the whole signal such as:

$$S_{est}(\omega) = \sum_{i=1}^{N_R} \frac{G_i(\omega)H_i(\omega)^*}{G_i(\omega)G_i(\omega)^*} S \ , \tag{1}$$

where ω is the angular frequency, S_{est} is the real Fourier transform of estimated source, $G(\omega)$ is the real Fourier transform of the observed signal, $H(\omega)$ is the real Fourier transform of the signal calculated in the synthetic model, $S(\omega)$ is the synthetic source used to compute $H(\omega)$, N_R is the number of receivers and * denotes the conjugate. The main issue of this method is that inaccuracies in the synthetic model, and consequently in the calculated data, are integrated in the estimated source. This leads to inaccuracies in the update models and then to the final models resulting from inversion. For a given dataset, one or more efficient sources can be estimated, if the source is considered to be stable from a shot to another or not, but estimate the source for each shot for large multisource-multireceiver data can quickly result in a significant additional numerical cost.

We have shown in the previous section that MUSC system is able to generate high quality 2D experimental seismograms which will be more usable for imaging method validations if the source waveform is constant during an experiment. As shown by Bretaudeau et al. (2011), the source waveform injected in the reduced-scale model by the piezo-electric source is not similar to the selected theoretical one. Figures 5(c) and 5(d), in previous section, show multiple wavefront following the first arrival wavefronts. After Bretaudeau et al. (2011), these multiples are generated inside the conical adapter of the piezo-electric source before being injected in the model. This naturally raises question about the ability of MUSC system to provide reproducible source, at least, during a complete multisource-multireceiver experiment. To evaluate the reproducibility of the source impact, several numerical and

15

physical modeling were performed on the same *F50 pure* homogeneous epoxy-resin block as in previous section.

In a first step, ten realizations have been acquired on this model with a similar geometry setup: 120 receivers positions with an increment $\Delta r = 1\ mm$ and a minimum source-receiver offset of $O = 10\ mm$. The numerical wavelet sent to the piezoelectric transducer source is a Ricker function with a central frequency of $100\ kHz$ and $t_0 = 0.03\ ms$. Each data set was filtered using a low-pass Butterworth filter with a cutoff frequency $\omega_c = 250\ kHz$ to remove noises and tapered at begin and end using a cosine taper function of width $w = 0.03\ ms$. Then, a 3D/2D geometrical spreading correction was applied using the *hybrid* method with with a linear offset dependent ratio $r = O/O_{max}$, where O_{max} is the maximum source receiver offset. Figure 8(a) shows the resulting central trace ($o = 70\ mm$) of each realization compared to a reference central trace resulting from average of traces for the same offset. The good agreement between central traces and the reference is a first validation of the reproducibility of the source in a same experiment. In a second step, to go further, a unique source wavelet is estimated using equation 1. The source wavelet estimation takes into account the vertical components of the ten experiments together and allows to obtain a mean effective source wavelet (figure 9(a)). This effective source is very different of the theoretical one with a strong asymmetry around the main pulse at t_0 and a large sequence of source echo from $t = 0.04\ ms$ to the end of the time window. Since the numerical modeling does not take into account the quality factor, the distortion of the source can be exaggerated but still exists. This source wavelet, applied to all synthetic signals should reproduce experimental data if the real source wavelet is the same for all experiments. The resulting traces are presented in figure 9(b) which shows that corrected synthetic seismograms are in good agreement with the experimental ones.

16

These last results, based on an average estimated source wavelet show that the effective impulse source emitted by the transducer in the MUSC system measurement bench is stable enough to ensure a robust reproducibility of the source for a complete physical experiment with multiple source and receiver positions. Therefore, concerning the key issue of the source knowledge, experimental data acquired in the MUSC system can be efficiently processed by imaging methods like Full Waveform Inversion (FWI) with only one estimation step for all the multi-source and multi-receivers data.

Towards complex models and acquisitions

In the two previous sections, the geometrical spreading correction calibration and the source estimation have been done on a simple homogeneous block of F50 epoxy-resin. This approach facilitates developments and applications but limits the validation to a simple media with simple acquisition geometry. Thus, we consider here a more complex model, called *BiAlt* (figure 3. The acquisition is 120 mm long, centered on the central alteration of the model, and composes of 241 receivers with a spacing of $\Delta r = 0.5 \ mm$. 25 source positions are considered, ranging from 0 to 241 mm with a spacing $\Delta s = 1 \ mm$. Sources are Ricker with a central frequency $f_0 = 75 \ kHz$ and $t_0 = 0.03 \ ms$. A low-pass Butterworth filter ($\omega_c = 200 \ kHz$) and a cosine taper are applied to the data. Given that the top layer of the model is made of the same epoxy-resin as the homogeneous block, we applied the hybrid geometrical spreading correction with the same parameters. Corresponding synthetic data were generated using a two-dimensional SEM algorithm. Again, the quality factor is not took into account. Figure 10(a) shows the efficient source wavelet estimated from the 241×25 traces compared to the theoretical one. In this case, the estimated source wavelet seems more stable, *i.e.* more symmetric and with few and very low amplitude multiples.

17

This can be related, first to the lower central frequency of the source which may generate

less multiple in the conical adapter of the piezoelectric source, and second to the absorption

365 of the high attenuation of LAB1000 ignored in numerical modeling. Again, this estimated

source is applied to the synthetic data and the resulting traces for the first source are

shown in figure 10(b). Comparison experimental traces (black) and numerical traces com-

pute with the theoretical source wavelet (red) shows that the relative amplitude between P

and S wavefront are very different, in particular between intermediate and far offset, which

370 can be, again, related to a low quality factor for S-wave of the *LAB1000* epoxy-resin. Also,

a phase shift appears progressively and is clearly visible at far offset, denoting inaccuracy

in the P- and S- wave velocity estimation of the epoxy-resins. However, their is still a

good agreement between experimental traces and numerical ones. Given that the effective

source is estimated using a realistic multisource-multireceiver acquisition design over 25

375 source positions, this results confirms the stability of the source during large experimental

campaigns.

CONCLUSIONS

PLOTS

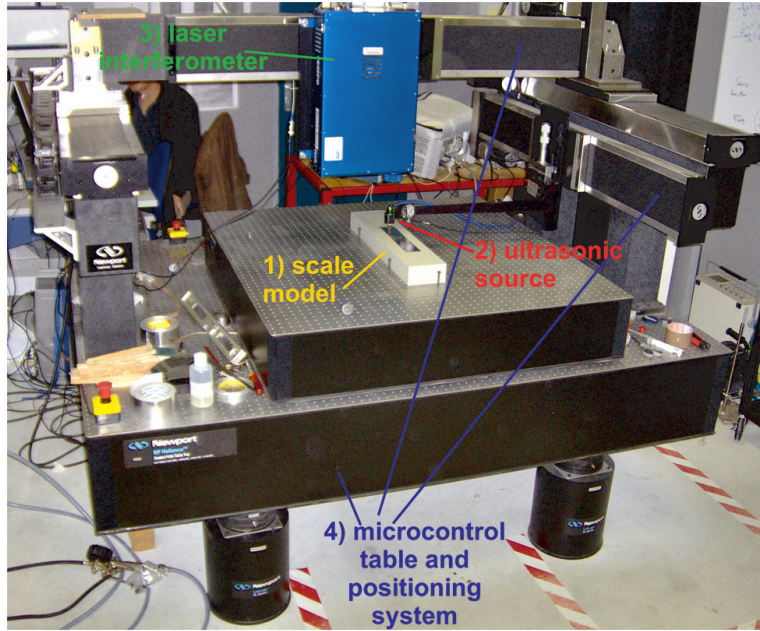**Equations**

Figures

18

Figure 1: Photograph of the MUSC ultrasonic laboratory (from Bretaudeau et al. (2013))with its four components: (1) a small-scale model of the underground, (2) an optical table with two automated arms moving above the model, (3) a laser interferometer recording ultrasonic wave propagation at the model surface,(4) a piezoelectric ultrasonic source generating ultrasonic waves in the model.
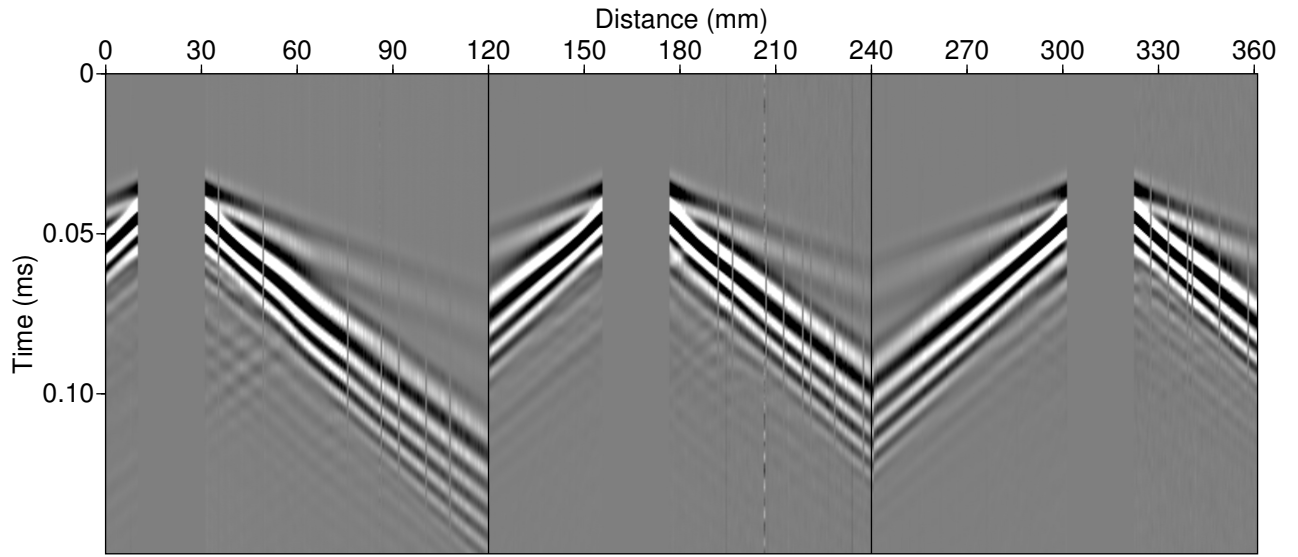
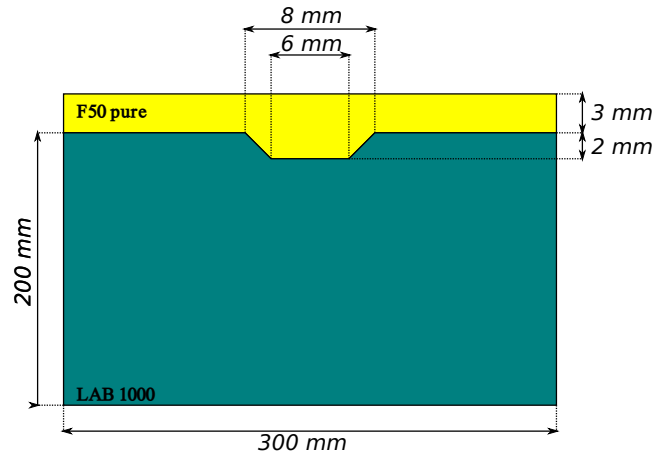Figure 2: Example of multi-source multi-receiver record on the MUSC system for a two-layer

model (bialt).

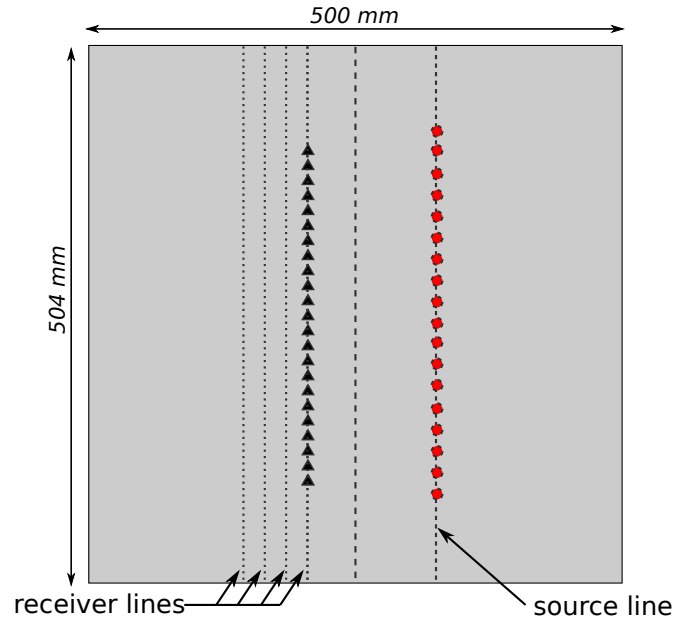Figure 3: Schematic representation of the so-called *BiAlt* model.

Figure 4: Schematic representation of the acquisition geometry used to generate experimental line-source, *i.e.* an equivalent of cylindrical source use in two-dimensional modeling. Black traingle and red circle represent receivers and sources, respectively.
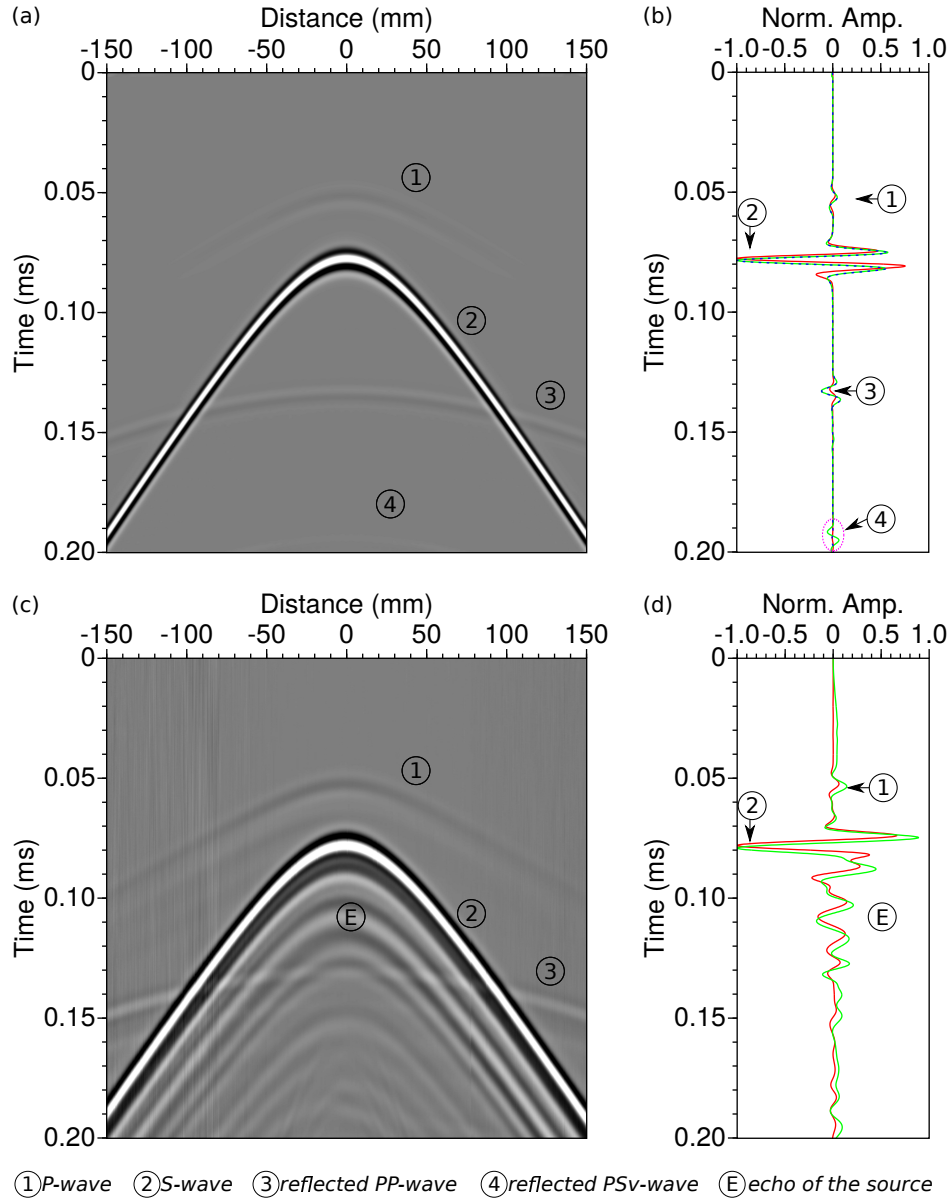
Figure 5: (a,b) Numerical modeling. (a) Resulting seismogram at one receiver position for the experimental line-source. (b) Comparison between point-source response in red (central trace of (a)), weighted stack response of(a) in green and line-source response from two-dimensional modeling in blue. (c,d) Same as (a) and (b) but for experimental modeling.
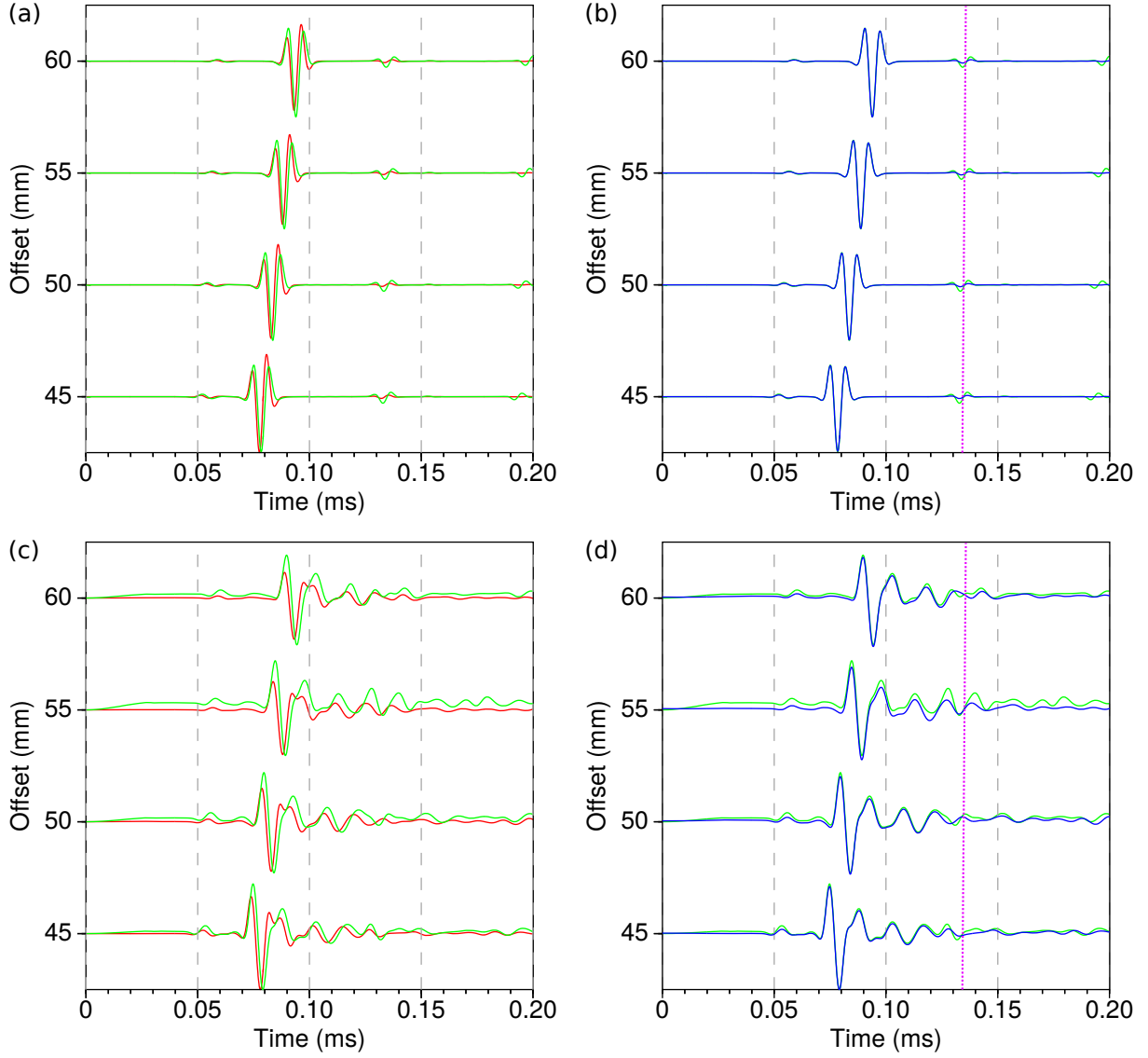
Figure 6: (a,b) Numerical modeling. (a) Comparison between synthetic seismograms for a point-source (red) and for a line source (green), for 45, 50, 55 and 60 mm source-receiver offsets respectively. (b) Comparison between synthetic seismograms for a line-source (green), and a point-source response corrected from geometrical spreading (blue) for same source-receiver offsets as (a) using the hybrid method with ratios $r = 0.35$, $r = 0.40$, $r = 0.45$ and $r = 0.50$ for offsets 45, 50, 55 and 60 mm, respectively . (c,d) Same as (a) and (b) for experimental modeling. The light-purple dotted lines pick PSv-wavefront.
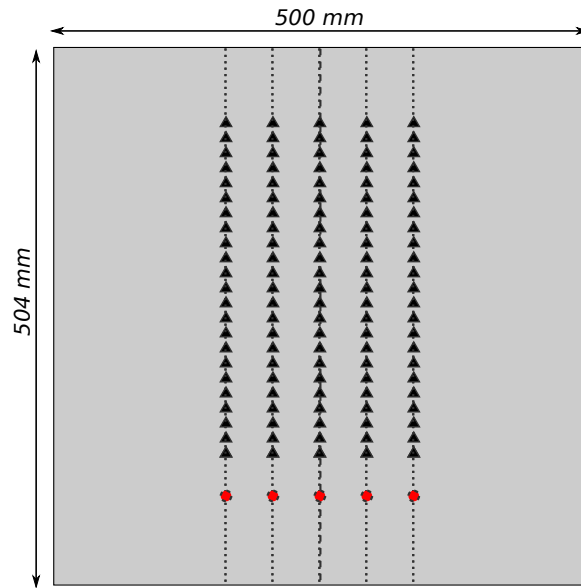
23

Figure 7: Schematic representation of the acquisition geometry used to assess the data reproducibility using the MUSC system. Black traingle and red circle represent receivers and sources, respectively.
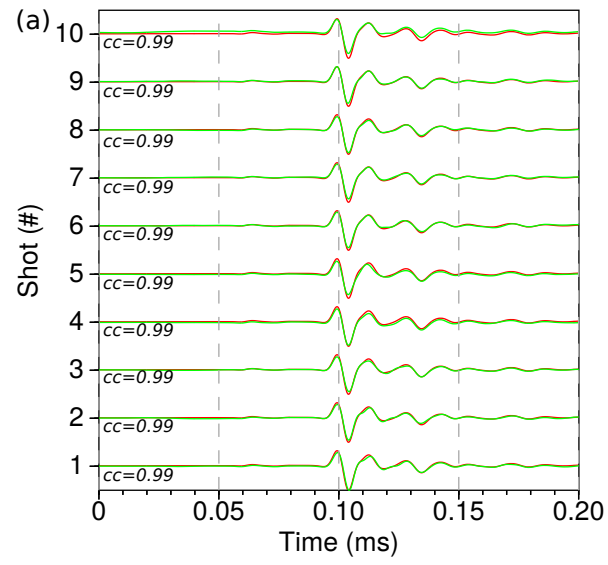
Figure 8: Central trace for each of the ten analogic experiment. **cc** gives the correlation factor of each central trace with respect to a mean central trace (green).
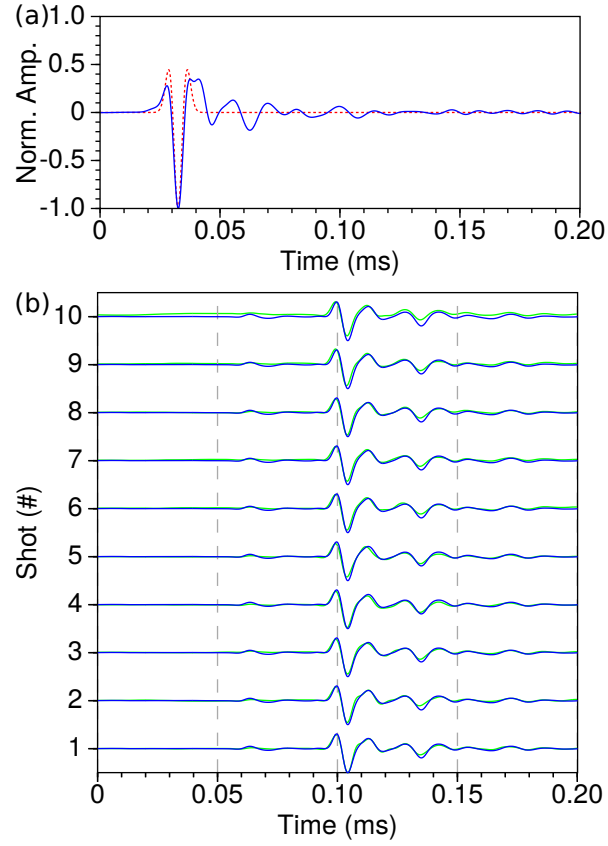
Figure 9: (a) Comparison between theoretical source send to the piezo-electric transducer (dashed red line) and the effective source injected in the model (blue line). (b) Comparison between experimental central traces and numerical ones using the effective source instead theoretical one.
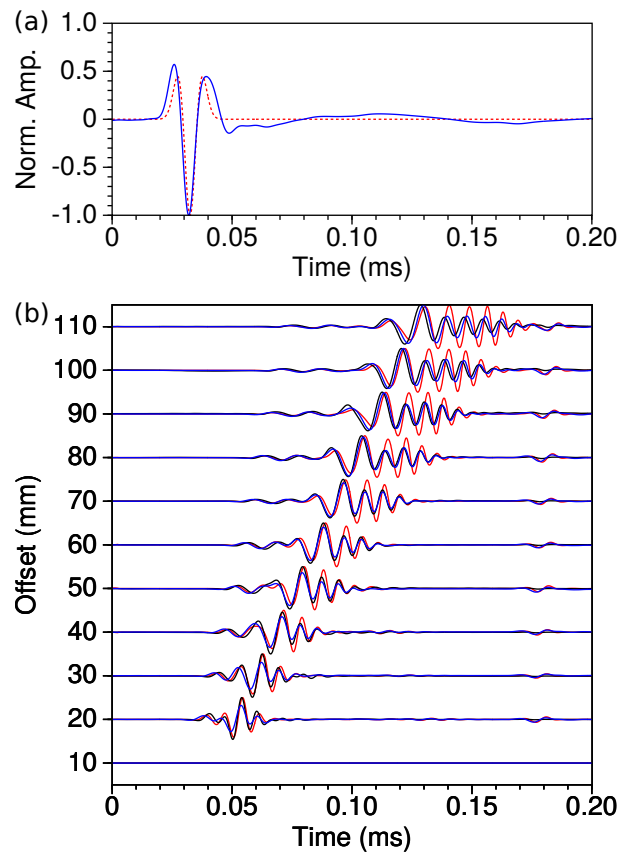
Figure 10: .

Tables

material	Field experiment scale	MUSC experiment scale	scales ratio
P waves velocity	V_{p0}	V_{p0}	1
S waves velocity	V_{s0}	V_{s0}	1
Time	T_0	$0.001\ T_0$	0.001
frequency	F_0	$1000\ F_0$	1000
Distance	D_0	$0.001\ D_0$	0.001
Wavelengh	D_0	$0.001\ D_0$	0.001

Table 1: example of possible scales ratio between field experiments and MUSC experiments when considering a ratio equal to 1 for the density and Quality factor.

material	Field experiment scale	MUSC experiment scale	scales ratio
P waves velocity	V_{p0}	$2V_{p0}$	2
S waves velocity	V_{s0}	$2V_{s0}$	2
Time	T_0	$0.001\ T_0$	0.001
frequency	F_0	$2000\ F_0$	2000
Distance	D_0	$0.001\ D_0$	0.001
Wavelengh	D_0	$0.001\ D_0$	0.001

Table 2: example of possible scales ratio between field experiments and MUSC experiments when considering a ratio equal to 2 for the density and Quality factor.

material	V_P (m/s)	V_S (m/s)	V_R (m/s)	ρ (kg/m^3)	Q
Aluminium	5630	3225	–	2700	–
F50 pure	2300	1030	965	1300	30
F50 200%	2820	1425	1328	1766	–
F50 240%	2968	1496	1388	1822	–
LAB1000	2850	1400	1310	1500	75

Table 3: Physical properties of some materials used to build small scale models. V_P, V_S and V_R are the P-wave velocity, S-wave and the Rayleigh wave velocity, respectively. ρ is the density and Q is the quality factor.

	90 mm	95 mm	100 mm	105 mm
$cc1_{init}$	0.702	0.725	0.728	0.728
$rms1_{init}$	0.794	0.760	0.762	0.774
$cc1_{final}$	0.940	0.953	0.951	0.949
$rms1_{final}$	0.358	0.317	0.325	0.343
$cc2_{init}$	0.954	0.987	0.988	0.988
$rms2_{init}$	0.304	0.162	0.155	0.154
$cc2_{final}$	–	–	–	–
$rms2_{final}$	–	–	–	–

Table 4: .

ACKNOWLEDGMENTS

REFERENCES

Bérenger, J. P., 1994, A perfectly matched layer for the absorption of electromagnetic waves: Journal of Computational Physics, **114**, 185–200.

Berkhout, A., D. Verschuur, and G. Blacquiere, 2012, Illumination properties and imaging promises of blended, multiple-scattering seismic data: a tutorial: Geophysical Prospecting, **60**, 713–732.

Bishop, T., K. Bube, R. Cutler, R. Langan, P. Love, J. Resnick, R. Shuey, and D. Spinder, 1985, Tomographic determination of velocity and depth in laterally varying media: Geophysics, **50**, 903–923.

Bohm, G., J. M. Carcione, D. Gei, S. Picotti, and A. Michelini, 2015, Cross-well seismic and electromagnetic tomography for co 2 detection and monitoring in a saline aquifer: Journal of Petroleum Science and Engineering, **133**, 245–257.

Bretaudeau, F., R. Brossier, D. Leparoux, O. Abraham, and J. Virieux, 2013, 2d elastic full-waveform imaging of the near-surface: application to synthetic and physical modelling data sets: Near Surface Geophysics.

Bretaudeau, F., D. Leparoux, and O. Abraham, 2008, Small scale adaptation of the seismic full waveform inversion method - application to civil engineering applications.: The Journal of the Acoustical Society of America, **123**.

Bretaudeau, F., D. Leparoux, O. Durand, and O. Abraham, 2011, Small-scale modeling of onshore seismic experiment: A tool to validate numerical modeling and seismic imaging methods: Geophysics, **76(5)**, T101–T112.

Cristini, P., and D. Komatitsch, 2012, Some illustrative examples of the use of the spectral-element method in ocean acoustics.: Journal of the Acoustical Society of America.

Favretto-Cristini, N., A. Tantvereva, P. Cristini, B. Ursin, D. Komatitsch, and A. Aizen-

berg, 2013, Numerical modeling of zero-offset laboratory data in a strong topographic environment: results for a spectral-element method and a discretized kirchhoff integral method: Earthquake Science.

Festa, G., and J. Vilotte, 2005, The Newmark as velocity-stress time-staggering: an efficient PML implementation for spectral element ssimulation of elastodynamics: Geophysical Journal International, **161**, 798–812.

Forbriger, T., L. Gross, and M. Schafer, 2014, Line-source simulation for shallow-seismic data. part 1: theoretical background: Geophysical Journal International, **198**, 1387–1404.

French, W. S., 1974, Two-dimensional and three-dimensional migration of model-experiment reflection profiles: Geophysics, **39(3)**, 265–277.

Geuzaine, C., and J. Remacle, 2009, Gmsh: a three-dimensional finite element mesh generator with built-in pre- and post-processing facilities.: International Journal for Numerical Methods in Engineering, **79**, 1309–1331.

Guofeng, L., L. Yaning, R. Li, and M. Xiaohong, 2013, 3d seismic reverse time migration on gpgpu: Computers & Geosciences, **59**, 10–23.

Hilterman, F., 1970, Three-dimensional seismic modeling: Geophysics, **35**, 1020–1037.

Howes, E., L. Tejada-Flores, and L. Randolph, 1953, Seismic model study: Journal of the Acoustical Society of America, **25**, 915–921.

Hulbert, G. M., and T. J. Hughes, 1990, Space-time finite element methods for second-order hyperbolic equations: Computer Methods in Applied Mechanics and Engineering, **84**, 327–348.

Isaac, J. H., and D. C. Lawton, 1999, Image mispositioning due to dipping ti media: A physical seismic modeling study: Geophysics, **64**, 1230–1238.

Karniadakis, G. E., 1989, Spectral element simulations of laminar and turbulent flows in

complex geometries: Applied Numerical Mathematics, **6**, 85 – 105. (Special Issue on Spectral Multi-Domain Methods).

Komatitsch, D., and J. Tromp, 1999, Introduction to the spectral-element method for three-dimensional seismic wave propagation: Geophysical Journal International, **139**, 806–822.

Komatitsch, D., S. Tsuboi, and J. Tromp, 2005, The spectral-element method in seismology.

Komatitsch, D., J. P. Vilotte, R. Vai, J. M. Castillo-Covarrubias, and F. J. Sánchez-Sesma, 1998, The Spectral Element Method for Elastic Wave Equation: Application to 2-D and 3-D Seismic Problems: International Journal for Numerical Methods in Engineering, **45**, 1139–1164.

Korczak, K. Z., and A. T. Patera, 1986, An isoparametric spectral element method for solution of the navier-stokes equations in complex geometry: Journal of Computational Physics, **62**, 361 – 382.

Levander, A., 1988, Fourth-order finite-difference p-sv seismograms: Geophysics, **53**, 1425–1436.

Lysmer, J., and L. A. Drake, 1972, A finite element method for seismology: Methods in computational physics, **11**, 181–216.

Moczo, P., J. Kristek, and L. Halada, 2004, The finite-differences method for seismologists: An introduction: Comenius University, Bratislava.

Morozov, I., 2004, Crustal scattering and some artefacts in receiver function images: Bulletin of the Seismological Society of America, **94**, 1492–1499.

Patera, A. T., 1984, A spectral element method for fluid dynamics: Laminar flow in a channel expansion: Journal of Computational Physics, **54**, 468–488.

Perez Solano, C., D. Donno, and H. Chauris, 2014, Alternative waveform inversion for surface wave analysis in 2-d media: Geophysical Journal International, **198**, 1359–1372.

Pratt, R. G., 1990, Frequency domain elastic wave modeling by finite differences: A tool for cross-hole seismic imaging.: Geophysics, **55**, 626–632.

———, 1999, Seismic waveform inversion in the frequency domain, Part 1: Theory and verification in a physical scale model: Geophysics, **64**, 888–901.

Rieber, F., 1936, Visual presentation of elastic wave patterns under various structural conditions: Geophysics, **1**, 196–218.

Robertsson, J., J. Blanch, and W. Symes, 1994, Viscoelastic finite-difference modeling.: Geophysics, **59**, 1444–1456.

Saenger, E. H., and T. Bohlen, 2004, Finite-difference modeling of viscoelastic and anisotropic wave propagation using the rotated staggered grid: Geophysics, **69**, 583–591.

Saenger, E. H., N. Gold, and A. Shapiro, 2000, Modeling the propagation of elastic waves using a modified finite-difference grid: Wave Motion, **31**, 77–92.

Sarkar, D., A. Bakulin, and R. L. Kranz, 2003, Anisotropic inversion of seismic data for stressed media: Theory and a physical modeling study on berea sandstone: Geophysics, **68**, 1–15.

Schafer, M., L. Gross, T. Forbriger, and T. Bohlen, 2014, Line-source simulation for shallow-seismic data. part2: full-waveform inversion – a synthetic 2-d case study: Geophysical Journal International, **198**, 1405–1418.

Seron, F. J., F. J. Sanz, M. Kindelan, and J. I. Badal, 1990, Finite-element method for elastic wave propagation: Communications in applied numerical methods, **6**, 359–368.

Stekl, I., and R. G. Pratt, 1998, Accurate visco-elastic modeling by frequency-domain finite differences, using rotated operators.: Geophysics, **63**, 1779–1794.

Tran, K. T., M. McVay, M. Faraone, and D. Horhota, 2013, Sinkhole detection using 2d full seismic waveform tomography: Geophysics, **78**, R175–R183.

475 Tromp, J., D. Komatitsch, and Q. Liu, 2008, Spectral-element and adjoint methods in seismology.: Commun Comput Phys.

Virieux, J., 1986, P-sv wave propagation in heterogeneous media: velocity-stress finite-difference method: Geophysics, **51**, 889–901.

Virieux, J., and S. Operto, 2009, An overview of full-waveform inversion in exploration 480 geophysics: Geophysics, **74**, WCC1WCC26.

Wirgin, A., 2004, The inverse crime: ArXiv Mathematical Physics e-prints. (Provided by the SAO/NASA Astrophysics Data System).

Wong, J., K. W. Hall, E. V. Gallant, R. Maier, M. Bertram, and D. C. Lawton, 2009, Seismic physical modeling at university of calgary: CSEG recorder, **34**.